Computational models for simulations of lithium-ion battery cells under constrained compression tests

CrossMark

Mohammed Yusuf Ali [a], Wei-Jen Lai [b], Jwo Pan [a,*]

[a] Department of Mechanical Engineering, The University of Michigan, Ann Arbor, MI 48109, USA
[b] Department of Materials Science and Engineering, The University of Michigan, Ann Arbor, MI 48109, USA

HIGHLIGHTS

- Develop computational models for simulations of lithium-ion battery cells.
- Model the multi-scale buckling of lithium-ion battery cells.
- Model the formation of kinks and shear bands in lithium-ion battery cells.
- Model the buckling of cover sheets and justify the length selection of cell specimens.
- Model the void compaction, plastic deformation and load-displacement curves.

ARTICLE INFO

ABSTRACT

In this paper, computational models are developed for simulations of representative volume element (RVE) specimens of lithium-ion battery cells under in-plane constrained compression tests. For cell components in the finite element analyses, the effective compressive moduli are obtained from in-plane constrained compressive tests, the Poisson's ratios are based on the rule of mixture, and the stress−plastic strain curves are obtained from the tensile tests and the rule of mixture. The Gurson's material model is adopted to account for the effect of porosity in separator and electrode sheets. The computational results show that the computational models can be used to examine the micro buckling of the component sheets, the macro buckling of the cell RVE specimens, and the formation of the kinks and shear bands observed in experiments, and to simulate the load−displacement curves of the cell RVE specimens. The initial micro buckling mode of the cover sheets in general agrees with that of an approximate elastic buckling solution. Based on the computational models, the effects of the friction on the deformation pattern and void compaction are identified. Finally, the effects of the initial clearance and biaxial compression on the deformation patterns of the cell RVE specimens are demonstrated.

© 2013 Elsevier B.V. All rights reserved.

1. Introduction

Lithium-ion batteries have been considered as the solution for electric vehicles for the automotive industry due to its lightweight and high energy density. The major design considerations of lithium-ion batteries involve electrochemistry, thermal management and mechanical performance. The electrochemistry has been widely studied since it directly determines the battery performance and its life cycle. Different active materials on electrodes give different types of lithium-ion batteries. However, the basic chemical reactions of the cells are similar. For automotive applications, the mechanical performance is of great importance for crashworthiness analyses. Research works were conducted on the safety performance of the battery cells under mechanical tests such as nail penetration tests, round bar crush tests, and pinch tests, for example, see Refs. [1–5]. Many research works were also conducted to understand and model the phenomena related to intercalation induced stresses, diffusion, debonding, cracking, and the effect of the coatings due to reaction in the lithium-ion batteries, for example, see Refs. [6–13]. However, these research works mainly focused on electrodes or separators and understandably do not cover the global mechanical behavior of battery cells, modules and packs.

Sahraei et al. [14] conducted a series of mechanical tests and computational modeling works on commercial $LiCoO_2$/graphite

* Corresponding author. Tel.: +1 734 764 9404; fax: +1 734 647 3170.
E-mail addresses: mdyusuf@umich.edu (M.Y. Ali), weijen@umich.edu (W.-J. Lai), jwopan@gmail.com, jwo@umich.edu (J. Pan).

Nomenclature

α	kink angle
θ	shear band angle
θ_i	initial shear band angle
θ_f	final shear band angle
h_s	shear band height
d	kink length
w	cell thickness
ϕ	Gurson yield function for porous materials
f	void volume fraction; it is defined as the ratio of the volume of voids to the total volume of the material
f_0	initial void volume fraction
r	relative density of a material; it is defined as the ratio of the volume of matrix material to the total volume of the material
q	effective macroscopic Mises stress
p	macroscopic hydrostatic pressure
σ_y	flow stress
σ_{y0}	yield stress
$\bar{\varepsilon}_m^{pl}$	average equivalent plastic strain
q_1, q_2 and q_3	fitting parameters
$\mathbf{S}$	deviatoric part of the macroscopic Cauchy stress tensor
$\mathbf{\Sigma}$	macroscopic Cauchy stress tensor
ν_i	Poisson's ratio of the i-th component for rule of mixture (ROM)
V_i	volume fraction of the i-th component for ROM
$\sigma_{y_{Gurson}}$	adjusted flow stress of the matrix
PEEQ	equivalent plastic strain
RVE	representative volume element
n	number of waves
m	number of half waves
l	length of the cell
k	the spring constant of the elastic foundation on one side of the beam and is defined as the lateral force per unit plate length per unit deflection of the neighbor components in the out-of-plane direction
E	modulus of elasticity
b	width of the specimen
h	thickness of the neighbor components
Π	potential energy of the system
I	moment of inertia
v	deflection of the beam in the y direction
P	compressive force
$h_{cover\ sheet}$	thickness of the cover sheet
h_{anode}	thickness of the anode
$h_{cathode}$	thickness of the cathode
$h_{separator}$	thickness of the separator
$h_{foundation}$	thickness of the foundation (neighbor components)

cells used for cell phones. The results indicate that the compressive mechanical behavior is characterized by the buckling and densification of the cell components. Other testing and modeling data available were also conducted on commercial $LiCoO_2$ cylindrical or prismatic battery cells [15,16]. However, this information is of limited use for researchers to model the mechanical performance of automotive high-voltage $LiFePO_4$ battery cells and modules for crashworthiness analyses. Sahraei et al. [14] indicated that computational effort is quite significant to model local buckling phenomenon of battery cells under in-plane compression. Therefore, macro homogenized material models of the representative volume elements (RVEs) for both the battery cells and modules have to be developed for crashworthiness analyses with sacrifice of the accuracy at the micro scale. Other than dealing with the multi-physics problem, one of the challenges of developing the computational models for the battery behavior is to deal with different models at different length scales as indicated in Ref. [14]. Therefore, understanding the basic mechanical behavior of the lithium-ion batteries for automotive applications is very important to develop macro homogenized material models for representative volume elements (RVEs) of cells and modules for efficient crashworthiness analyses.

Recently, Lai et al. [17,18] investigated the mechanical behaviors of lithium−iron phosphate battery cells and modules by conducting tensile tests of individual cell and module components, constrained compression tests of RVE specimens of dry cells and modules, and a punch test of a small-scale dry module specimen. Their results of in-plane tensile tests of the individual cell components indicate that the active materials on electrodes have a very low tensile load carrying capacity. For in-plane constrained compression tests of cell RVE specimens, the results indicate that the load carrying behavior of cell RVE specimens is characterized by the buckling of cells with a wavelength approximately in the order of the thickness of the cells and the final densification of the cell components. They also tested module RVE specimens with different heights and the results indicate that the load carrying behavior of module RVE specimens is also characterized by the buckling of cells with a wavelength

approximately in the order of the thickness of the cells and the final densification of the module components but relatively independent of the height of the tested specimens. In addition, they investigated the effects of adhesives between cells and foam/aluminum heat dissipater sheets on the mechanical behavior of module RVE specimens. The results indicate that the adhesive
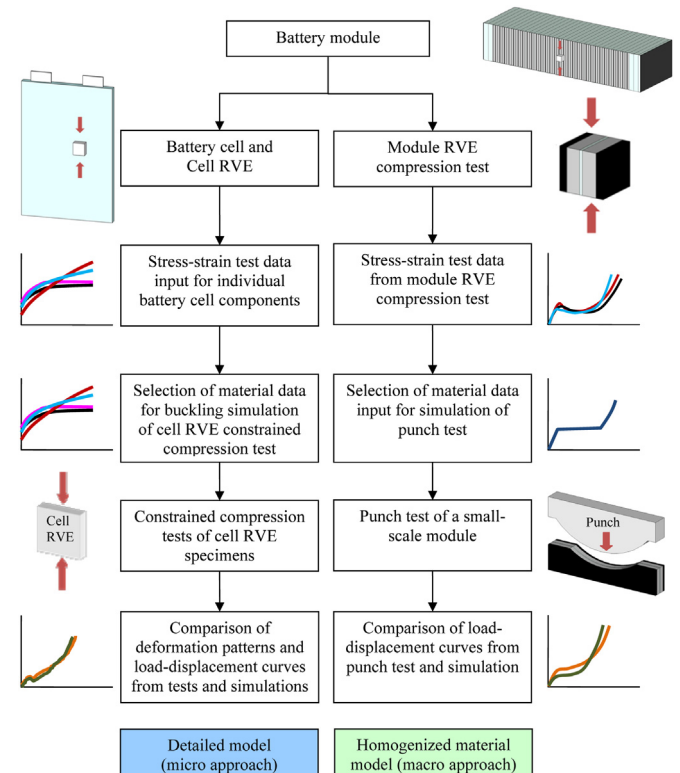

Fig. 1. A schematic view of the approaches for computational model developments.

slightly increases the compressive load carrying capacity of the module RVE specimens. Their SEM images of the active materials on electrodes and the results of in-plane compressive and out-of-plane compressive tests suggest the total volume fraction is up to 40% for the microscopic gaps between cell components and the porosity of the separators and the active materials on electrodes. Based on the compressive nominal stress—strain curves in the in-plane and out-of-plane directions, their work suggests that the lithium-ion battery cells and modules can be modeled as anisotropic foams or cellular materials.

The current study is focused on developing the computational models for simulations of RVE specimens of lithium-ion battery cells under in-plane constrained compression tests based on the work of Lai et al. [17] and then comparing the computational results with those of the tests. Fig. 1 shows a schematic view of the approaches of the developments of the computational models. Two approaches are used for the modeling of these battery cells and modules: a detailed model (micro approach) and a less detailed model (macro approach). This investigation will focus on the detailed modeling of a cell RVE specimen of lithium-ion batteries. In the detailed model, the pouch cell battery is modeled as a layered composite and the RVE material nominal stress—strain response is obtained based on the properties of the cell components of layered anode, cathode, separator and cover sheets. The less detailed models were investigated in a companion study [19] to address the length scale issue in mechanical modeling of the batteries. In those less detailed models, a small-scale battery module was considered as a homogenized material based on the response of the physical testing of the module RVE specimens [18]. Both approaches are useful to investigate the mechanical behavior of lithium-ion pouch cell batteries and modules.

The purpose of this detailed model investigation is twofold: one is to enhance understanding of the mechanical behavior of lithium-ion battery cells used for automotive applications and the other is to pave the groundwork for the development of user material models to represent the battery cells and modules by homogenized materials which are a subject of the future research. Finite element models can be used to simulate the tensile tests for multi-layered cell and module RVE specimens. However, a simple estimation scheme for tensile behavior is presented in Ref. [18] based on the rule of mixture (ROM) for composite and thus the tensile behavior of battery cells will not be addressed here. In this investigation, the compressive behavior of cell RVE specimens under quasi-static in-plane compression tests is investigated using the ABAQUS explicit finite element solver [20]. In this paper, the experimental results for cell RVE specimens under in-plane compression tests are first reviewed briefly for understanding the physical deformation pattern of the porous cell RVE specimens. Next, the Gurson's model for porous material is presented for characterization of the separator and the electrodes with the active materials. Then the available material data are discussed and adopted for the input of the computational model. The details of the computational model are presented. The computational results of the deformation pattern and nominal stress—strain behavior are then compared with the test results. Based on the detailed computational results, the micro buckling modes of the component sheets are identified and an approximate elastic buckling solution of a beam with a rigid boundary on one side and an unattached elastic foundation on the other side is developed and used to examine the micro buckling mode of the cover sheets for justification of the selection of the length of the cell RVE specimens used in the tests in Ref. [17]. Based on the computational model, the effects of the friction between the
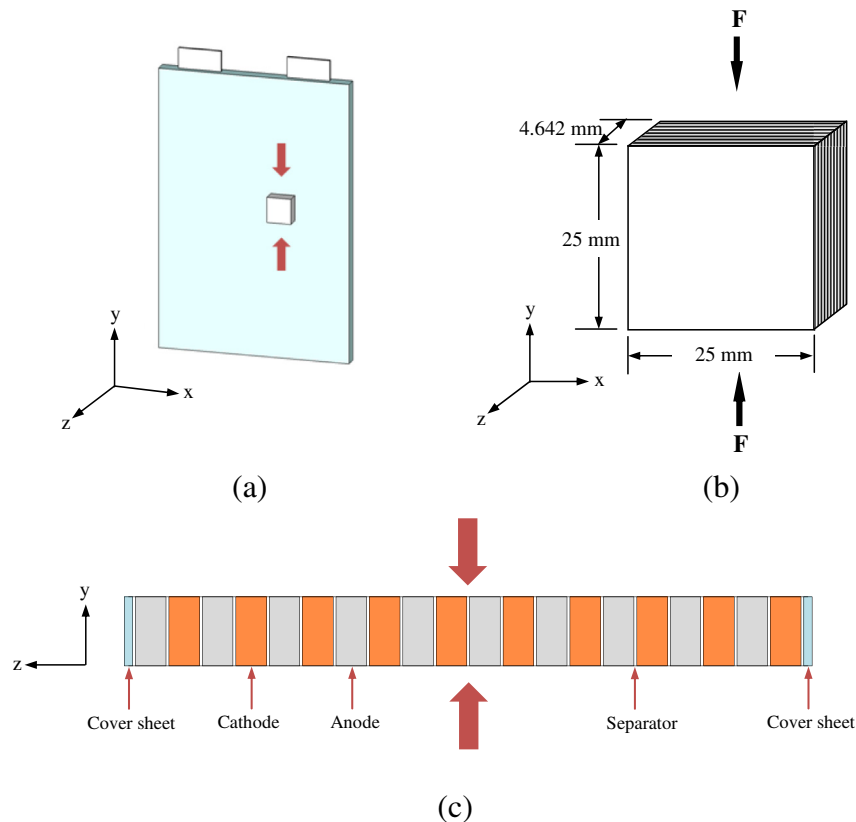

Fig. 2. A schematic of (a) a pouch cell and (b) a cell RVE specimen with the dimensions, and (c) a side view of a small portion of a ten-unit cell RVE specimen showing the individual cell components. The large arrows indicate the compressive direction.

cell components and the constrained surfaces on the deformation pattern, plastic deformation, void compaction, and the load–displacement curve are examined. The usefulness of the computational model is then presented by further exploring the effects of the initial clearance and biaxial compression on the deformation patterns of cell RVE specimens. Finally, some conclusions are made.

2. Experiment

A detailed description of the structure of a lithium-ion battery module used for this investigation can be found in Refs. [17,18]. Also note that the following definitions will be used throughout the paper. A *Single unit* cell represents a basic cell containing one cathode, one anode and a separator sheet with two aluminum cover sheets with two accompanying separator sheets. A *Ten unit* cell consists of ten basic cells containing ten cathode, ten anode, twenty one separator and two aluminum cover sheets. In this investigation, the ten unit cell is considered as a general cell RVE specimen that represents a typical assembled pouch cell.

Each cell consists of five major components: cover sheet, anode, cathode, separator and electrolyte. Since the electrolyte is difficult to handle during assembly due to the safety concern, all the cell and module RVE specimens tested in this study were made without electrolyte at the University of Michigan. Fig. 2(a) shows a schematic of a pouch cell with two cover sheets and a cell RVE specimen with the $x-y-z$ coordinate system. A cell RVE specimen with the dimensions is shown in Fig. 2(b). The pouch cell has a layered structure as schematically shown in Fig. 2(b). The z-coordinate is referred to as the out-of-plane coordinate whereas the x and y coordinates are referred to as the in-plane coordinates. Fig. 2(c) shows a side view of a small portion of a ten-unit cell RVE specimen showing the individual cell components. The assembly of the cell components in the generic cell RVE specimen as schematically shown in Fig. 2(c) may be slightly different from those in usual lithium-ion cells for convenience of assembly of the purchased cell components. However, generic cell RVE specimens with slightly different assemblies should have the similar buckling, kink and shear band mechanisms under constrained compression as discussed later due to their layered structures. Constrained compression tests were conducted for cell RVE specimens with the dimension of 25 mm × 25 mm × 4.642 mm. The details of the test

setup and results of the in-plane constrained compression tests are discussed in Ref. [17] and are briefly reviewed in the following.

Fig. 3 shows three nominal compressive stress–strain curves of the cell RVE specimens tested at a displacement rate of 0.5 mm min^{-1}. The specimens showed almost a linear behavior in the beginning with an effective elastic modulus of 188 MPa. Note that the effective elastic modulus obtained from the composite ROM is 190 MPa using the effective elastic moduli obtained from the nominal stress–strain curves of cell components under in-plane constrained compression tests. When the strain reaches about 2%, noticeable change of the slope takes place and the curves continue to increase gradually up to the strains of 34%. Some minor drops were observed during the stage after the linear region due to the development of kinks and shear bands as shown in the deformation patterns recorded as discussed later. The trends of all three curves are quite consistent.

Figs. 4(a)–(d) show the deformation patterns of a cell RVE specimen at the nominal strain of 1% in the initial linear stage, at the nominal strain of 2% where the slope changes, and at the nominal strains of 10% and 15%. Figs. 4(e) and (f) show the front and back views of the tested cell RVE specimen at the nominal strain of 34%. A careful examination of the deformation pattern shown in Fig. 4(a) indicates the initial linear stage corresponds to the development of smooth buckling for the cell components. As the displacement increases toward the nominal strain of 2% where the slope starts to level off, the cell RVE specimen shows the development of kinks or plastic hinges of the cell components against the walls, as indicated in Fig. 4(b). The presence of the kinks promotes the macroscopic shear band formation (strain localization in a narrow zone), as indicated in Fig. 4(b). The shear band formation creates a physical mechanism to accommodate efficiently for the compression displacement and hence induces the load drop. As the strain continues to increase, more kinks and shear bands form across the cell RVE specimen as shown in Figs. 4(c) and (d). Figs. 4(e) and (f) show the front and back views of the tested cell RVE specimen at the nominal strain of about 34%. As shown in the figures, the kinks are fully developed as folds and many shear bands can be identified. After the efficient compaction mechanism of shear band formation has been completed, further compression can only be accommodated by the micro buckling of the cell components outside the shear band regions, as marked in Figs. 4(e) and (f), and the compression in the shear band regions.

An idealized deformation process of the cell RVE specimen under an in-plane constrained compression test is proposed in Ref. [17] to explain the shear band formation and is briefly reviewed here. Figs. 5(a)–(c) show schematics of a cell RVE specimen before, during, and after the shear band formation under in-plane constrained compression, respectively. Figs. 5(d)–(f) show the detailed schematics of the shear band formation corresponding to Figs. 5(a)–(c), respectively. As shown in Fig. 5(a), the cell RVE specimen (shown in gray) forms shear bands (between two parallel dashed lines) to accommodate the volumetric reduction under constrained compression. During the deformation, the kink angle α (as shown in Fig. 5(e)) keeps deceasing from 90° toward to zero while the shear band angle θ (as shown in Fig. 5(e)) also decreases from the initial θ_i to the final θ_f by a small amount. In the shear band, the cell components are subjected to a compressive strain in the z' direction, a significant amount of the shear strain in the $y'-z'$ plane and a significant amount of rotation. Here, y' and z' represent the local material coordinates that are fixed to the material. Outside of the shear band, the cell components are subjected to compressive strains in the y and z directions. Once α reaches to zero, further compressive strains are achieved by the micro buckling of the cell components outside of the shear bands and the void reduction and shear in the shear band as θ continues to decrease. This is illustrated
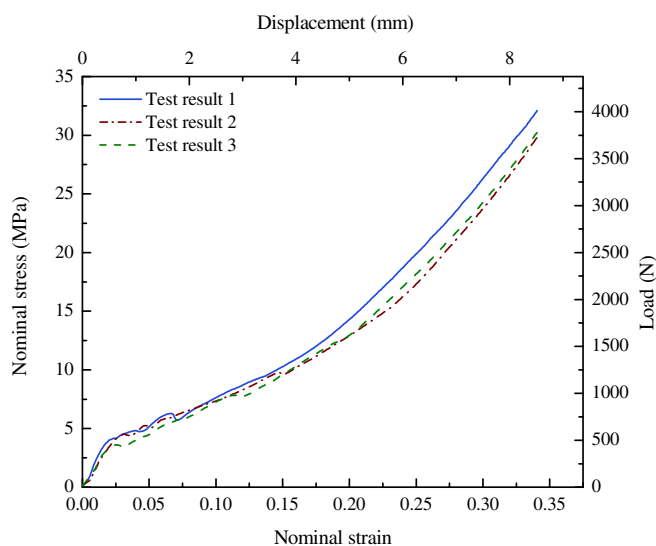

Fig. 3. Nominal compressive stress–strain curves of the cell RVE specimens tested at a displacement rate of 0.5 mm min^{-1} (nominal strain rate of 0.0003 s^{-1}).
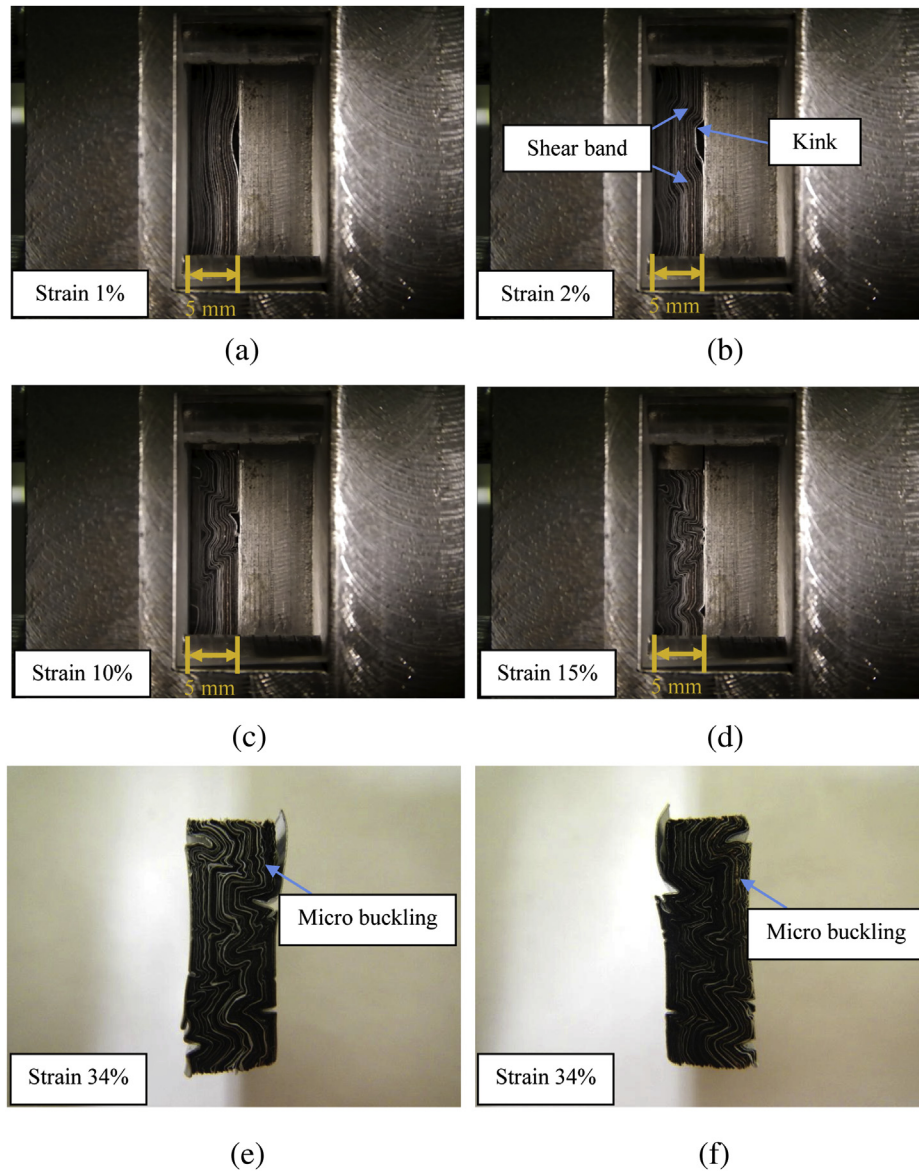
Fig. 4. Deformation patterns of a cell RVE specimen during a compression test at the displacement rate of 0.5 mm min^{-1}: (a) at the nominal strain of 1% in the initial linear stage, (b) at the nominal strain of 2% where the slope changes, (c) at the nominal strain of 10%, (d) at the nominal strain of 15%, (e) at the nominal strain of 34% after the test (front view), and (f) at the nominal strain of 34% after the test (back view).

in Figs. 5(c) and (f). It should be noted that Figs. 5(a)–(f) are idealized with the periodic shear band structures. In tests, the shear bands do not form at the same time and the shear band angle θ varies due to the imperfections of the specimens.

3. Gurson's yield function for porous materials

The anode and cathode for this investigation are graphite coated on copper foil and LiFePO$_4$ coated on aluminum foil, respectively. The copper foil has a thickness of 9 μm and the total thickness of the anode sheet is 0.2 mm. The aluminum foil has a thickness of 15 μm and the total thickness of the cathode sheet is 0.2 mm. Both the anode and cathode sheets are double-side coated. The separator is made of polyethylene with the porosity ranging from 36 to 44% and a thickness from 16 to 25 μm according to the manufacturer specification.

Fig. 6 shows SEM images of the graphite and LiFePO$_4$ on the anode and cathode sheets, respectively, reported in Lai et al. [17]. It should be noted that both active materials on electrodes are in a powder form held together by the binder and therefore possess a high degree of porosity as seen in the SEM images. It is not the intent of this paper to characterize the composition and morphology of the active materials on the electrodes. For example, the porosities of the active materials on the current collectors as shown in Figs. 6(a) and (b) are difficult to measure and characterize. However, the electrodes with the porous active materials can be computationally treated as homogenized porous sheets. The results of the tensile tests of the cell component sheets will be used to determine approximately the plastic parts of the stress–strain curves of the component sheets as homogenized materials, and the results of the constrained compression tests of the cell component specimens will be used to determine approximately the compressive moduli of the component sheets as homogenized materials as detailed later in this paper and in Lai et al. [17].

It should be mentioned that the electrode sheets are idealized as homogenized porous sheets in the micro computational models
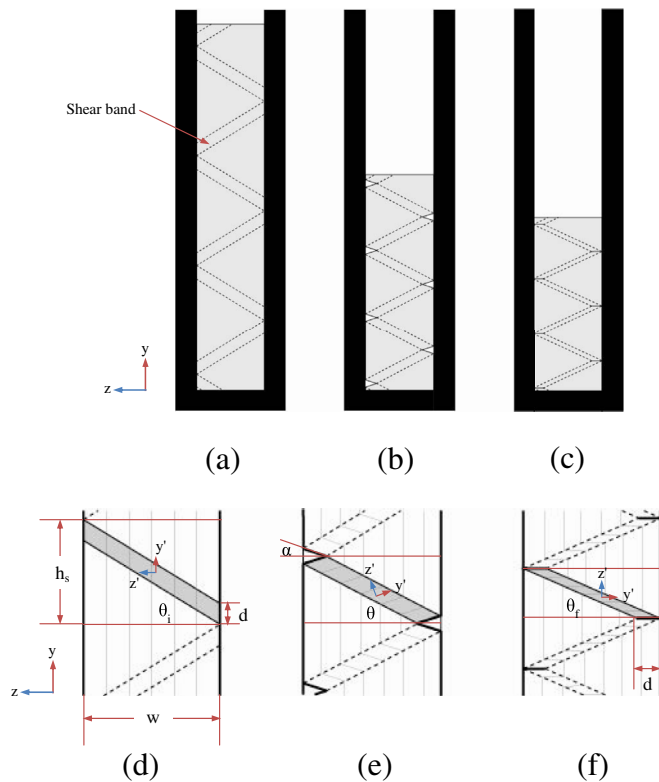
Fig. 5. Schematics of a cell RVE specimen (a) before, (b) during, and (c) after in-plane constrained compression. (d)–(f) are detailed schematics showing the shear band formation corresponding to (a)–(c), respectively. The y and z coordinates are the global coordinates and the y' and z' coordinates in (d)–(f) are the local material coordinates rotating with the cell components.

used for the cell RVE specimens in this paper and the computational effort is quite extensive. It is possible to consider the active materials on the current collectors as particles for the electrode sheets in computational models at smaller scales. However, this paper is focused on development of computational models at the scales of homogenized cell component sheets, and development of computational models at smaller scales is out of the scope of this paper. The Gurson's model for porous materials is adopted to model the electrode sheets with the active materials as homogenized materials in the finite element analyses. Also, the separator sheets used in the cell RVE specimens are manufactured with a high degree of porosity to hold electrolyte. Therefore, the Gurson's model for porous
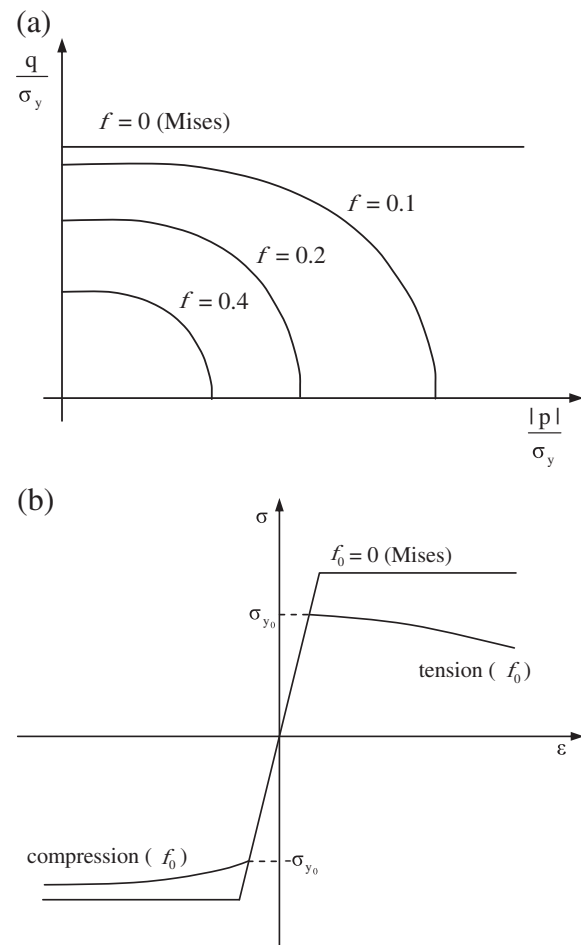

Fig. 7. (a). A schematic of the Gurson's yield contour in the normalized hydrostatic pressure (p) – Mises stress (q) plane [20]. (b). A schematic of uniaxial behavior of a porous material with a perfectly plastic matrix material and the initial void volume fraction f_0 [20].

materials is also adopted to model the separator sheets as homogenized materials in the finite element analyses. A brief description of the Gurson's model [20] is presented in the following.

Gurson [21] proposed a yield function ϕ for porous materials containing a small volume fraction of voids. In porous materials, the void volume fraction f is defined as the ratio of the volume of voids
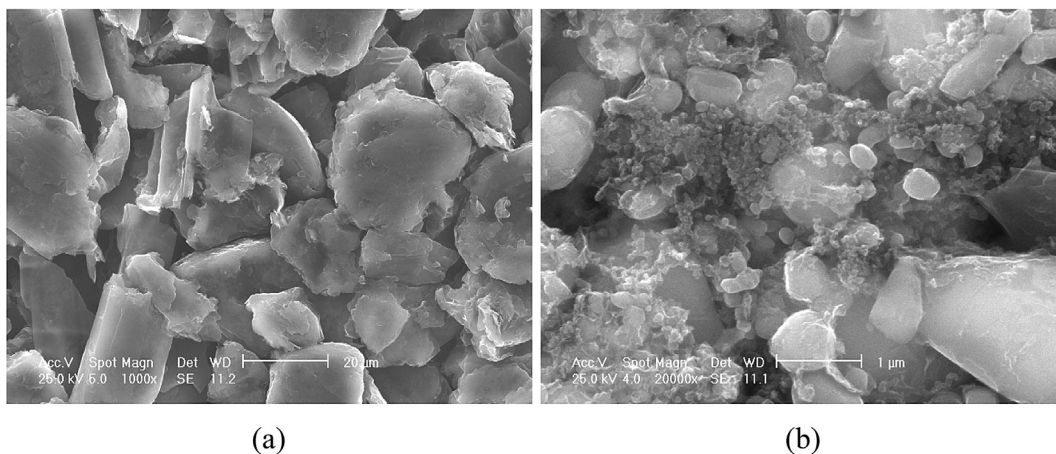

Fig. 6. SEM images of (a) graphite and (b) LiFePO$_4$ on the anode and cathode sheets, respectively.

to the total volume of the material. The relative density of a material, r, defined as the ratio of the volume of matrix material to the total volume of the material, can also be used. Note that $f = 1 - r$. The Gurson's yield function ϕ was later modified by Tvergaard [22] to the form

$$\phi = \left(\frac{q}{\sigma_y}\right)^2 + 2q_1 f \cos h \left(-q_2 \frac{3p}{2\sigma_y}\right) - \left(1 + q_3 f^2\right) = 0 \quad (1)$$

where $q \left(= (3\mathbf{S}:\mathbf{S}/2)^{1/2}\right)$ represents the effective macroscopic Mises stress, $p(=-\mathbf{\Sigma}:\mathbf{I}/3)$ represents the macroscopic hydrostatic pressure, σ_y represents the flow stress of the matrix material, which is expressed as a function of the average equivalent plastic strain $\bar{\varepsilon}_m^{pl}$ of the matrix for strain hardening materials, and q_1, q_2 and q_3 are the fitting parameters. Here, $\mathbf{S}$ represents the deviatoric part of the macroscopic Cauchy stress tensor $\mathbf{\Sigma}$. The macroscopic Cauchy stress $\mathbf{\Sigma}$ is based on the current configuration of a material element with voids. For $f = 0$ ($r = 1$), the material is fully dense, and the Gurson's yield function reduces to the Mises yield function. The model generally gives physically reasonable results only for $f < 0.1$ ($r > 0.9$). Tvergaard [22] introduced the fitting constants q_1, q_2 and q_3 to fit the numerical results of shear band instability in square arrays of cylindrical holes and axisymmetric spherical voids. One can recover the original Gurson's yield function by setting up $q_1 = q_2 = q_3 = 1$. In the current investigation, $q_1 = 1.5$, $q_2 = 1$, and $q_3 = q_1^2 = 2.25$ [20].

Fig. 7(a) shows a schematic of the Gurson's yield contour in the normalized hydrostatic pressure (p) − Mises stress (q) plane for porous materials in comparison with that of the Mises material model. The porous material model reduces to the Mises material model as the void volume fraction f reduces to zero. Fig. 7(b) shows a schematic of the uniaxial behavior of a porous material with a perfectly plastic matrix material and the initial void volume fraction f_0. Here the yield stress is denoted as σ_{y0}. The porous material softens in tension and hardens in compression. The porous material hardens in compression due to the reduction of the void volume fraction. Phenomenological hyperfoam and crushable foam material models are available in ABAQUS. However, more material input data are needed for these foam models and additional material data for the cell components are not available. Therefore, the Gurson's material model is adopted here for modeling the separator and the electrodes with the active materials.

4. Available material data for cell components

Tensile tests were conducted for the individual cell components such as anode, cathode, separator and cover sheets, and the test results were discussed in detail in Lai et al. [18]. In-plane constrained compression tests were also conducted for the anode, cathode, separator, and cover sheets to estimate the compressive elastic moduli, and the test results were discussed in detail in Lai et al. [17]. Although these tests are constrained compression tests, only the apparent elastic part of the stress–strain responses appear to be useful to obtain the effective compressive elastic moduli for individual components. The effective compressive elastic moduli may account for the local micro buckling that occurs at a very small load level for each component sheet and has indistinguishable impacts to the measurable macroscopic response. Due to the compressive loading of the cell RVE specimens, the effective compressive elastic moduli are thus used for the electrodes, separator and cover sheets in the finite element analyses of the cell RVE specimens under constrained compression tests.

Table 1
Material properties used in the finite element analyses.

	Tensile modulus (MPa)	Effective compressive modulus (MPa)	Tensile yield stress (MPa)	Poisson's ratio
Anode, graphite/Cu	4700	83	2.11	0.21 ($f = 0\%$) 0.17 ($f = 20\%$) 0.13 ($f = 40\%$)
Cathode, Li-FePO$_4$/Al	5100	275	1.48	0.21 ($f = 0\%$) 0.17 ($f = 20\%$) 0.14 ($f = 40\%$)
Separator	500	90	10.53	0.25 ($f = 44\%$)
Cover sheet	5600	575	9.74	0.41

For elastic–plastic materials, the plastic strain hardening behavior is essential for the input of elastic–plastic finite element analyses. For the current investigation, the elastic–plastic tensile stress–strain data for the components obtained in Ref. [18] are used to define the strain hardening behavior due to the difficulties to obtain such data under uniaxial 'unconstrained' compression tests. For the ABAQUS solver, the tensile tests data must be converted to the true stress and true strain format for elastic–plastic finite element analyses. There is no simple way to convert the engineering stress–strain curves of the anode, cathode and separator sheets with high porosity. The conversion to the true stress–strain curve is based on the usual assumption of plastic incompressibility for metal plasticity for lack of the detailed information on the detailed microstructure of the anode, cathode and separator. With the composite rule of mixture for the void and matrix and the assumption of the constant total volume of the void and matrix, the engineering stress–strain curve is converted to the true stress–strain curves. The anode and cathode fail at very low strains. The separator is very thin and is expected not to contribute significantly to the overall load carrying capacity of cells and modules. Therefore, the conversion to the true stress–strain curve with the plastic incompressibility seems to be a reasonable option for lack of further information.

The tensile and effective compressive moduli, tensile yield stress and Poisson's ratio of the cell components are listed in Table 1. For the linear part of each stress–strain curve, the modulus is calculated based on each data point with respect to the origin of the stress–strain curve. A stable average value for a range of the strain of the apparent linear behavior is selected as the tensile modulus for that specific material. The yield stresses for the materials of the cell components are selected where the stresses deviate from the apparent linear ranges. Poisson's ratios of 0.33 for copper, 0.33 for aluminum, 0.45 for polymer and 0.2 for the active layers are used to obtain the effective Poisson's ratio for the separator, anode, cathode, and cover sheets using the composite rule of mixture (ROM). The effect of the void volume fraction on the Poisson's ratio is estimated by treating the void as a component with zero Poisson's ratio using the ROM as

$$\nu_{ROM} = \sum_{i=1}^{n} \nu_i V_i \quad (2)$$

where ν_i and V_i are the Poisson's ratio and the volume fraction of the i-th component, respectively. Table 1 lists the Poisson's ratios

Table 2
Thicknesses and densities of the battery cell components.

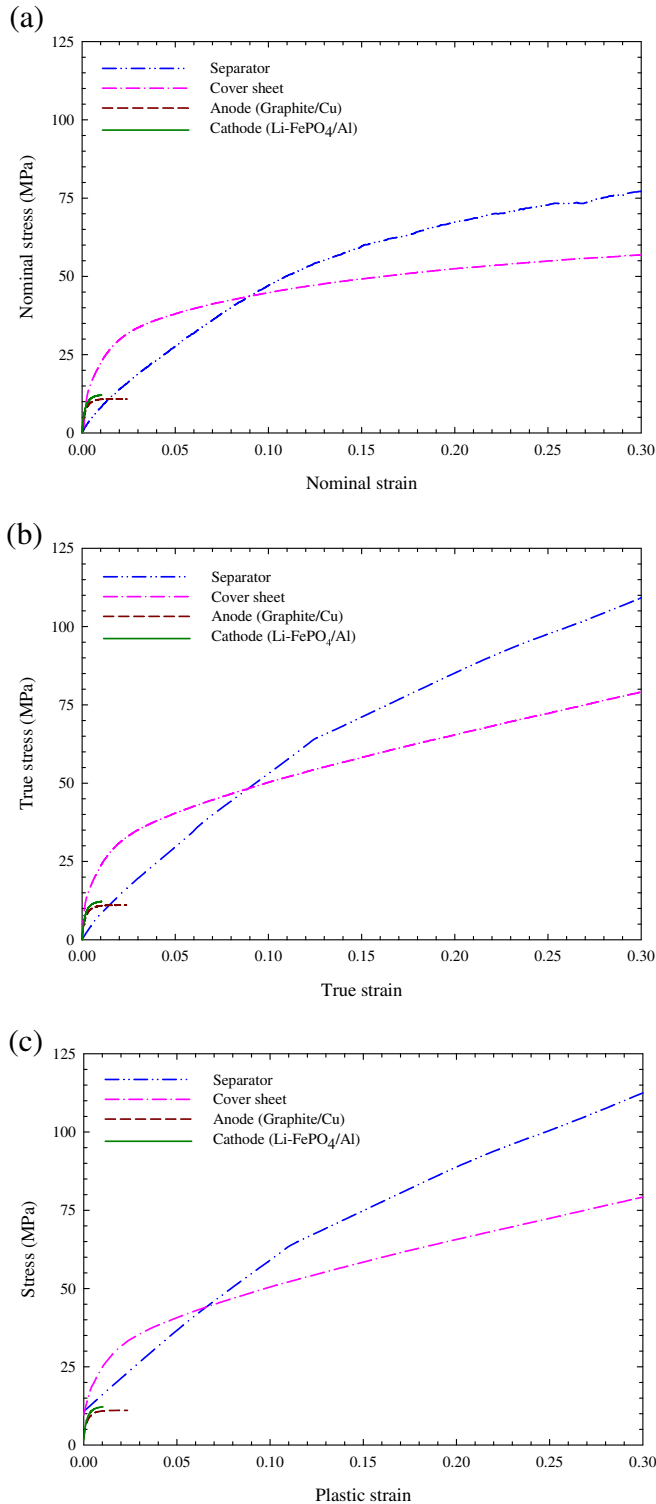|	Thickness, mm	Density, kg m^{-3}
Anode, graphite/Cu	0.2	934
Cathode, Li–FePO$_4$/Al	0.2	1712
Separator	0.02	795
Cover sheet	0.111	1338

(a)

(b)

(c)

Fig. 8. (a) The representative tensile nominal stress–strain data of the cell components obtained from Ref. [18], (b) estimated true stress–strain data based on (a), and (c) the stress–plastic strain curves of the cell components used in the finite element analysis.

for the cell components for different values of the initial void volume fraction f. The Poisson's ratios listed for anode and cathode in Table 1 are corresponding to the assumed void volume fraction f listed in the parenthesis. It should be noted that the void volume fractions of the active materials on electrodes are difficult to measure due to the fact that the graphite and lithium iron

phosphate particles are loosely bonded together by a weak binder. The void volume fraction 44% of the separator provided by the manufacturer is adopted here. The thicknesses and the densities of the cell components are also listed in Table 2.

Figs. 8(a) and (b) show the representative tensile nominal and true stress–strain data of the cell components, respectively, and Fig. 8(c) shows the stress–plastic strain curves of the cell components used in the finite element analyses. For the electrodes, the stress–plastic strain curves are provided up to the strain of failure in the tests. In ABAQUS, the stresses are kept constant outside the input strain range. In this case, this represents a perfectly plastic extension of the stress–plastic strain curves of the electrodes since they are apparently flat near the failure strains. This automatic extension of the input material data is used to avoid numerical issues that may arise due to error tolerance check used in regularizing the user-defined data in ABAQUS/explicit code.

As mentioned earlier for the micro and macro buckling analyses, the compressive elastic moduli of the cell components are used and are listed in Table 1. The cover sheet is modeled as the Mises material with the isotropic hardening rule of ABAQUS and the stress–plastic strain curve shown in Fig. 8(c) is used. For the separator sheets, the initial void volume fraction f is set at 0.44 based on the manufacturer specification. The plastic behaviors for the cell components are provided based on the stress–plastic strain curves shown in Fig. 8(c). The strain hardening behavior for the matrix material is obtained by scaling the tensile stress–plastic strain curves using the ROM as

$$\sigma_{y_{Gurson}} = \frac{\sigma_y}{1-f} \tag{3}$$

where σ_y and $\sigma_{y_{Gurson}}$ represent the flow stress and adjusted flow stress of the matrix, respectively. The stress–plastic strain curve based on equation (3) will be referred as 'adjusted strain hardening curve'. It should be mentioned again that the stress–plastic strain curves are estimations based on the available information. Many assumptions are made to obtain these curves. One goal of this investigation is to understand the physical mechanisms of these RVE specimens under constrained compressive tests. The details of the various aspects of compression tests simulations for cell RVE specimens are described in the following sections.

5. Computational models

The results of the compression tests of cell RVE specimens show that the layers of the RVE specimens are deformed by multi-scale buckling phenomenon − both layer micro buckling and global macro buckling. Ideally, in a confined space with no clearance and only with the presence of the porosity in the separator and the active materials on the electrodes, the dense parts of the layers (copper foils in anodes, aluminum foils in cathodes, and aluminum and polymers in cover sheets) would get the room for buckling only by compressing the relatively softer and porous active materials on electrodes and separator layers laterally or in the out-of-plane direction. However, the initial microscopic gaps between the cell components also allow some rooms for buckling. The following approach is adopted and tested in developing the buckling model presented here. As the load increases, the local buckling of the individual sheets of the specimens develops and then the kinks of the cell components start to form laterally adjacent to the wall of the fixture. The kinematics of development of kinks and shear bands is an efficient way to compact these porous sheets with plastically incompressible inner copper or aluminum foils. Based on the experimental observations [17], the cell global buckling or shear bands come from the plastic hinges or sharp bending due to the rigid constraint of the fixture wall and the module
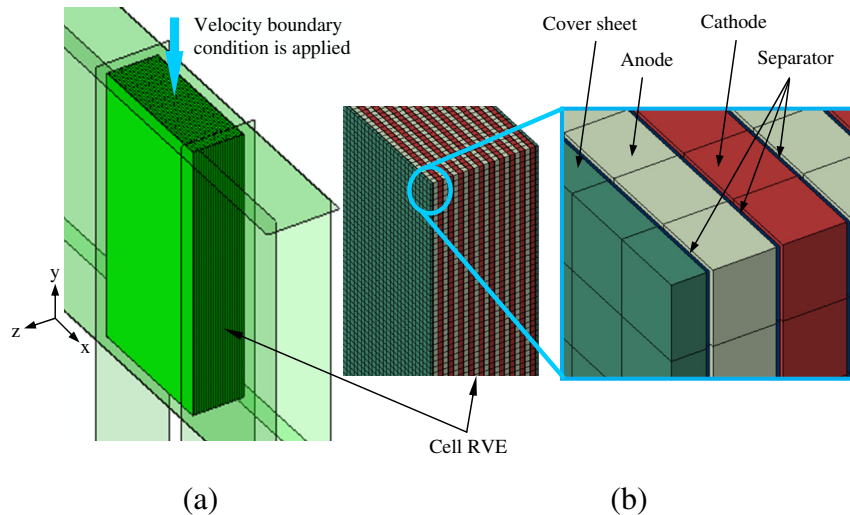
Fig. 9. (a) The finite element model setup for a cell RVE specimen under constrained compression, and (b) detailed views of the meshes where the anode, cathode and cover sheets are modeled by linear hexahedral solid elements and the separator sheet is modeled by linear quadrilateral reduced integration shell elements.

global buckling comes from the smooth bending due to a more relax environment from the soft foam padding. The formation of these kinks and shear bands in computational simulations is the key to properly simulate the buckling behavior of the cell RVE specimens under constrained compression tests.

The simulation of the cell RVE (ten units) specimens under compression tests will be presented here. The similar approach can be used for module RVE specimens under compressive loading to estimate the nominal stress–strain response that can be used as an input for a less detailed modeling [19]. Fig. 2(b) shows a schematic of a cell RVE specimen with the dimensions. It should be noted that the stack-up of the cell components gives a total thickness of 4.642 mm. However, the constrained compression test fixture has a confinement dimension of 25 mm × 25 mm × 5 mm. In the beginning of the compression test, a clearance of 0.358 mm was present in the lateral or thickness direction, and is modeled accordingly in the finite element analyses.

Fig. 9(a) shows the finite element model setup for a cell RVE specimen compression test using the ABAQUS/Explicit commercial finite element code. The x–y–z coordinate system is also shown. The explicit finite element solver is used for this simulation for a better contact stability among all the thin sheets during the buckling and under large deformation. The vertical length 25 mm and the thickness 4.642 mm of the finite element model are similar to the cell RVE specimen. For computational efficiency, only a half of the cell RVE specimen width of 25 mm is used in the finite element model. However, it should be noted that the symmetric boundary condition was not applied in the model due to the nature of the problem. The nominal stress vs. nominal strain curves of computational simulations will be compared with those of the tests.

The compression test fixture is made of steel that has a very high stiffness compared to the cell components. Therefore, the confinement surfaces are assumed to be rigid and modeled by planar rigid surfaces. In the finite element model setup, the specimen mesh is surrounded by six rigid surfaces. The rigid surfaces contacting with the edges of the cell RVE component sheets with the normals in the x and y directions have zero clearance. The rigid surfaces contacting the cover sheets with the normal in the z direction are 5 mm apart and provide a total of 0.358 mm initial lateral clearance with 0.179 mm on each side. The reference nodes of all the rigid surfaces except the top one have six degrees of freedom constrained. The top rigid surface can only move in the vertical direction and is given a velocity boundary condition. The general contact algorithm of ABAQUS/Explicit is used to model the contact interaction between the surfaces of the cell components that contact with one another and with the rigid surfaces. All the contact surfaces are assumed to be in friction contact with each other and an appropriate value of the coefficient of friction is used in the simulations as a fitting parameter. Fig. 9(b) shows detailed views of the meshes of each layer. The anode, cathode and cover sheets are modeled by linear hexahedral full integration solid elements (C3D8 of ABAQUS). Only a single layer of elements are used to model each layer and a mesh size of Δx = 0.25 mm and Δy = 0.25 mm is used. For the cathode and anode sheets, Δz = 0.2 mm. For the cover sheets, Δz = 0.111 mm. The thin separator is modeled by linear quadrilateral reduced integration shell elements (S4R of ABAQUS) with a thickness of 0.02 mm for convergence and computational efficiency.

The compression test speed of 0.008 mm s^{-1} is considered as a quasi-static condition. Using the explicit dynamics solver to model a quasi-static event requires some special considerations. It is computationally impractical to model the process by a time step to satisfy the Courant–Fredrich–Levy condition of numerical stability. A solution is typically obtained either by artificially increasing the loading rate or the speed of the process in the simulation, or increasing the mass of the system, or both. A general recommendation is to limit the impact velocity to less than 1% of the wave speed of the specimen, and a mass scaling of 5–10% is typical to achieve a desirable stable time increment. Also the kinetic energy of the deforming specimen should not exceed a small fraction (1–5%) of the internal energy throughout the quasi-static analysis. The densities of the cell components are very low and the mesh size in this simulation is fine enough to capture the micro and macro buckling behaviors. Therefore, for a reasonable computational time, the finite element analysis is conducted at a speed of 200 mm s^{-1} and with a uniform mass scaling of 100 times of the actual mass. The deformation speed and the kinetic energy are very low and meet the recommendations of the quasi-static analysis for the explicit solver even though a higher mass scaling is used for computational efficiency. Different percentages of mass scaling were examined. The results showed some impact on the initial part of the stress–strain response up to a strain of about 1.5% and the results are generally comparable.
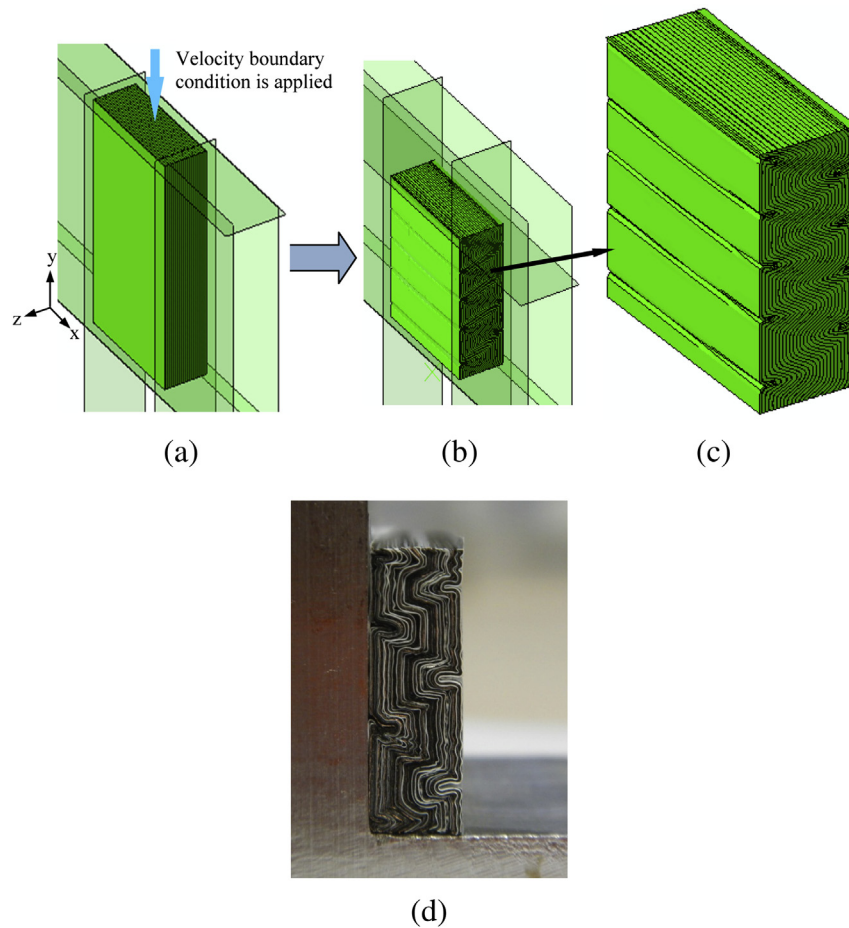
Fig. 10. (a) A cell RVE half model is confined by six rigid surfaces, (b) the deformed shape of the model after the compressive displacement is applied (with the effective elastic compressive modulus and $f = 0.2$ for the electrode sheets with the active materials at the nominal strain of 34%), (c) a zoom-in view of (b), and (d) a deformed cell RVE specimen after the in-plane compression test.

6. Computational results

Fig. 10 shows the initial and deformed shape of the battery cell model under quasi-static in-plane compression and the corresponding experimental results. Initially, the cell RVE model is confined by six rigid surfaces as described earlier as shown in Fig. 10(a). The top rigid surface is moved downward in the $-y$ direction with a velocity boundary condition. Fig. 10(b) shows the deformed shape of the model after the compressive displacement boundary condition is applied and held with the initial void volume fraction of $f = 0.2$ for the electrodes with the active materials at the nominal strain of 34%. In this case, the initial void volume fraction of $f = 0.2$ is used in estimating the Poisson's ratios and adjusting the strain hardening curves for the anode and cathode sheets with the active materials. In the model, a coefficient of friction of 0.1 is adopted for all the contacting surfaces as a general value. Many simulations with multiple combinations of the parameters such as the void volume fraction and coefficient of friction were conducted. Only the combinations of parameters giving reasonable results will be presented here. Fig. 10(c) is a zoom-in view of (b). Fig. 10(d) shows a deformed cell RVE test specimen after the in-plane compression test. The cell RVE specimen after the compression test shown in 10(d) is one of the three cell RVE specimens tested. Note that a different tested specimen is shown in Fig. 4. The specimen showed here has a fairly regular buckling pattern and was selected for comparison of the buckling pattern with that of the computational results. Regular buckling patterns are obtained from

the computational models since these computational models do not have significant irregularities or imperfections. The buckling patterns of the deformed finite element model are found similar and comparable to that of the test specimen.

Figs. 11(i)–(vi) show successive snapshots of the deformation of the cell RVE specimen during the buckling simulation. Figs. 12(i)–(vi) show the successive snapshots of the equivalent plastic strain (PEEQ) of the cell RVE specimen during the buckling simulation. In Fig. 11(ii) for the strain of 1.7%, the cover sheets on both sides of the cell specimen appear to buckle independently but the buckling is restricted by the rigid walls. The computational results not shown here indicate that the five buckles shown in Fig. 11(ii) develop successively one by one from the top to the bottom and the softer neighbor separator, anode and cathode sheets buckle with the stiffer cover sheets. In Fig. 11(iii) for the strain of 3.4%, the buckling peaks or valleys appear to adjust and synchronize with the macro buckling mode of the cell RVE specimen as a homogenized beam or plate. The absolute value of the nominal stress starts to drop at the strain of about 2% with the increasing compressive nominal strain based on the computational results and this appears to be related to the starting of the macro buckling of the cell RVE specimen as a homogenized beam or plate.

Fig. 11(iv) for the strain of 11.9% shows that kinks start to form adjacent to the cover sheets and shear bands are formed between the opposite pairs of kinks. As shown in Figs. 11(v) and (vi) for the strains of 22.1% and 34%, respectively, the kinks become folds and the folds have different depths. The spacing between the folds in
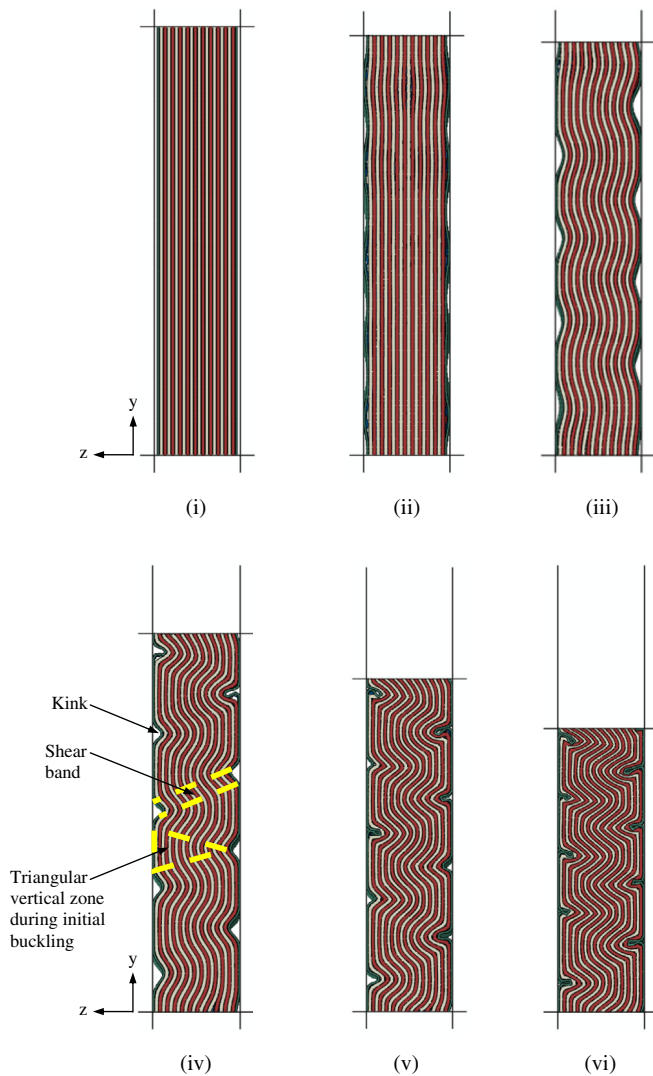
Fig. 11. The successive snapshots of the deformation of the cell RVE specimen during the buckling simulation at the nominal strains of (i) 0%, (ii) 1.7%, (iii) 3.4%, (iv) 11.9%, (v) 22.1% and (vi) 34%.

fact is not the same due to the friction and imperfections. The plastic hinges or bends of the cell components are found smoother in the computational models due to the large size of the elements in the finite element analyses compared to those of the tests where the bends are sharper with almost rectangular corners as shown in Figs. 4(d) and 10(d) for two different tested cell RVE specimens.

The shear bands are formed in the sheets between the two opposite kinks as schematically shown in Fig. 11(iv). As the deformation progresses, the shear bands in the computational models become slightly wider in the middle of the specimen compared to those of the tests due to the smoothing of the bends coming from the large element size in the finite element analysis. It should be noted that in order to capture the local bending more accurately, more layers of linear elements would have been appropriate to model each sheet. However, for computational efficiency and for a very high length to thickness ratio of each sheet, only a single layer of element is used for modeling each sheet to sufficiently capture the micro and macro deformation patterns.

The compaction of the voids in the components and microscopic gaps between the components, along with the initial clearances, allows room for further compression in a confined space. The kinks

grow up to certain depths and the surfaces collapse with further compressive loading as shown in Fig. 11(v). On the other hand, the stack of sheets that apparently are vertical between the two kinks on the same side are carrying loads by further deformations as shown in Figs. 11(iv)–(vi) and 12(iii)–(vi). The shape of this vertical zone across the thickness direction appears to be triangularly shaped whose apex is at the tip of the kink on the opposite side. Fig. 12(vi) shows that at the end of the compression, the values of the PEEQ are higher near the top of the specimen compared to those near the bottom. This can be attributed to the friction effect on the top portion due to the progress of compressive deformation.

Figs. 13(i) and (ii) show the distributions of the void volume fraction at the nominal strains of 8.5% and 34% of the constrained compression simulation, respectively. Only the void volume fractions of the anode and cathode sheets of the cell RVE specimen are displayed in these plots. Fig. 13(i) shows that during the deformation at the nominal strain of 8.5%, the voids along the outer boundaries of the shear bands where large bending occurs are consumed. Fig. 13(ii) shows that at the end of the compression at the nominal strain of 34%, the void volume fraction decreases more near the top of the specimen compared to that near the bottom. This can be attributed to the friction effect on the top portion due to the progressive nature of the compressive deformation.

Fig. 14 shows a comparison of the nominal stress–strain curve from the finite element analysis with that of the test results obtained from Lai et al. [17]. As mentioned earlier, the nominal stress–strain curve of the finite element analysis is based on the Gurson's material model with the initial void volume fraction $f = 0.2$ for the electrodes with the active materials and a friction coefficient of 0.1 based on a parametric study. The results of the parametric study show that the formation of the kinks and shear bands affects the stress where the slope of the nominal stress–strain curve of the computational results changes whereas a higher coefficient of friction raises the nominal stress to a higher value at a large strain. The results of the parametric study will not be reported here for brevity. The SAE 60 class filter has been used to post-process the computational stress–strain responses to filter the computational noise if present and for consistency in comparing the curves from computations [20]. The computational results show that the stresses drop slightly after the first noticeable global buckling at a strain of about 2% and this is in agreement with the experimental results. After reaching a strain of about 2%, the global buckling for the cell RVE specimen as a homogeneous beam begins. The stress then gradually increases as the densification or compaction continues as the strain increases. The results are compared fairly well with the test results in general. However, the computational response drops slightly after the strain of 25%.

The importance of the establishment and validation of the detailed computational model in this investigation can be demonstrated by exploring two example cases in order to visualize the effect of clearance and biaxial compression on the deformation patterns of cell RVE specimens under constrained compression. Only the deformation patterns of the two example cases are briefly presented here for demonstrating the usefulness of the computational model to understand the underlying physics of the cell RVE specimens under constrained compression.

The effect of the initial clearance on the shear band formation of a cell RVE specimen is demonstrated by using three initial clearances of zero, 0.358 mm (for the current model) and 0.716 mm in the finite element analyses. Figs. 15(a)–(c) show the deformation patterns of the cell model under quasi-static in-plane compression for the three clearance cases at the nominal strain of 34%. As the initial clearance in the finite element models decreases from 0.716 mm to 0.358 mm and then to zero, the number of kinks increases, the kink depth decreases, and the number of shear bands
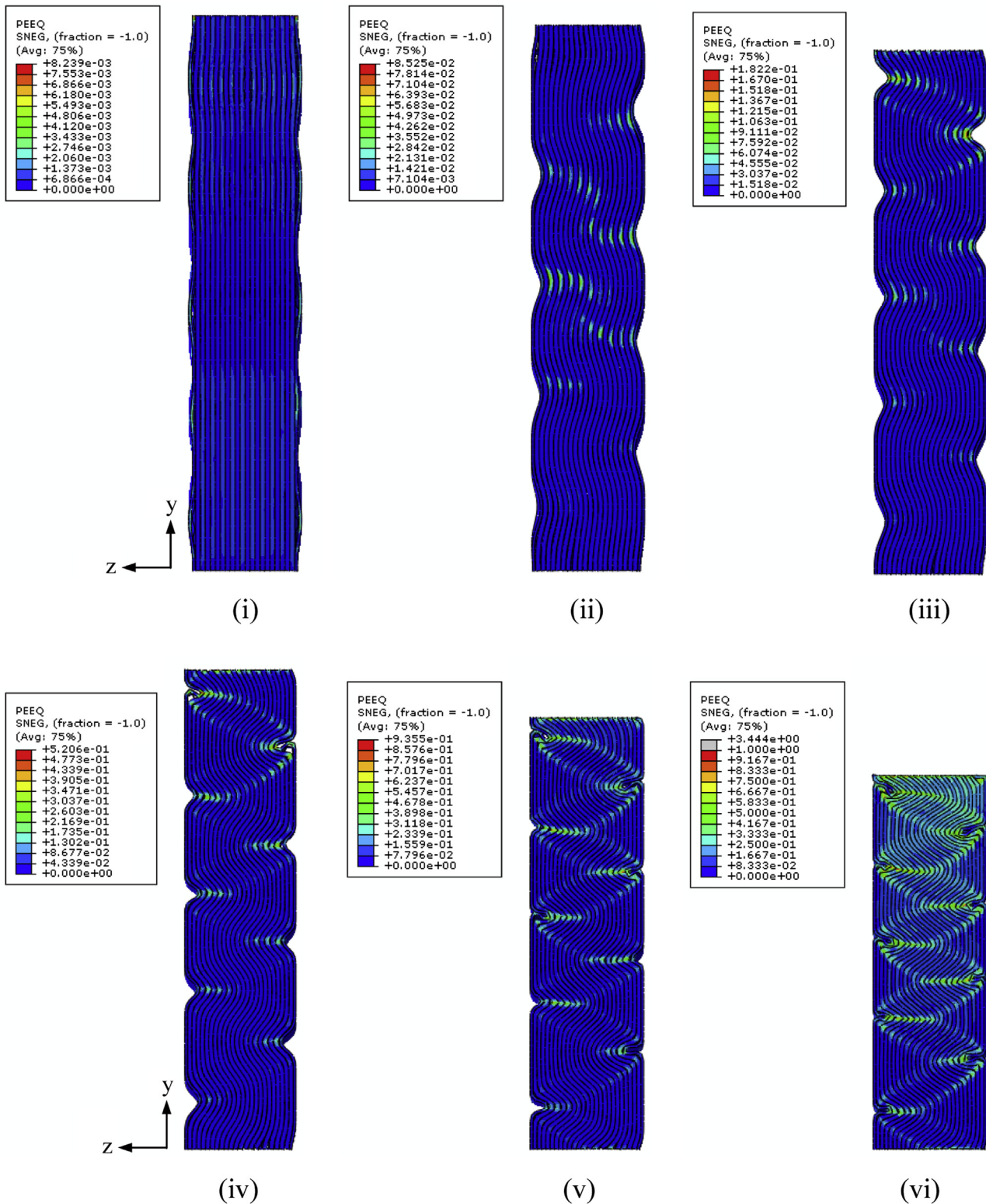
Fig. 12. The successive snapshots of the equivalent plastic strain (PEEQ) of the cell RVE specimen during the buckling simulation at the nominal strains of (i) 1.7%, (ii) 3.4%, (iii) 6.8%, (iv) 13.6%, (v) 23.8% and (vi) 34%.

increases from 8, 10 to 15, respectively. The details of the computational results will be reported with the corresponding experimental results in the future.

Fig. 16 shows the deformation pattern of a cell RVE specimen under equal biaxial constrained compression based on the model shown in Fig. 10(a). Here, the top and front rigid surfaces are moved downward in the −y direction and horizontally in the −x direction, respectively, with the velocity boundary conditions such that compressive nominal strains are equal in both x and y directions. The kinks and shear bands are formed inclined to both x and y
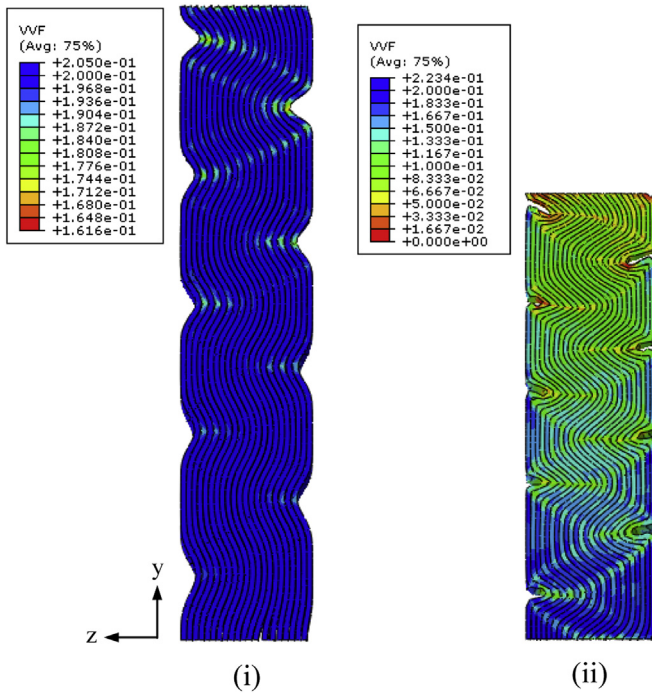
Fig. 13. The distributions of the void volume fraction at the nominal strains of (i) 8.5% and (ii) 34% of the constrained compression simulation. Only the void volume fractions of the anode and cathode sheets of the cell RVE specimen are shown.

15 shear bands   10 shear bands   8 shear bands

(a)   (b)   (c)

Fig. 15. The deformation patterns of a battery cell under quasi-static in-plane compression for three initial clearances of (a) zero, (b) 0.358 mm of the current model and (c) 0.716 mm at the nominal strain of 34%. The finite element models are similar to the model described in Fig. 10(a) with different initial clearances.

directions in Fig. 16. The number of kinks and shear bands on side S is about half compared to that of the side L due to the length ratio of one half for sides S and L in the computational model. Fig. 16 also shows the pattern of interactions of the shear bands initiated from sides L and S. The details of the computational results will be reported with the experimental results for biaxial compression in the future.

7. Discussions

Based on the experimental observations of the cell RVE specimens under in-plane constrained compression, the physical
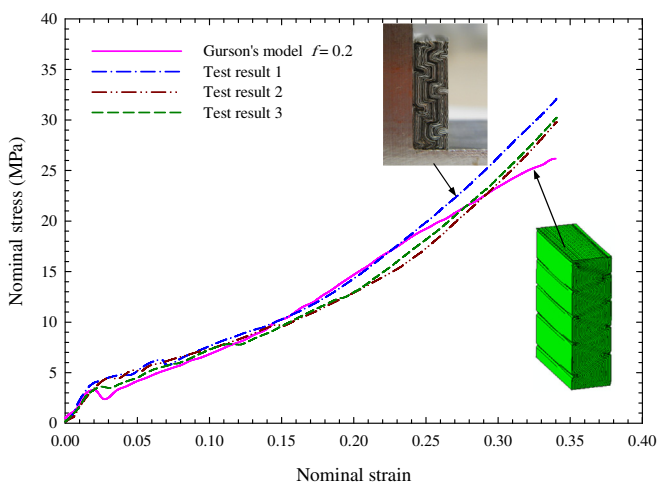

Fig. 14. A comparison of the nominal stress−strain curve from the finite element analysis using the Gurson's material model with those of the test results. In the finite element analyses, all the contact surfaces are assumed to be in friction contact with a friction coefficient of 0.1.
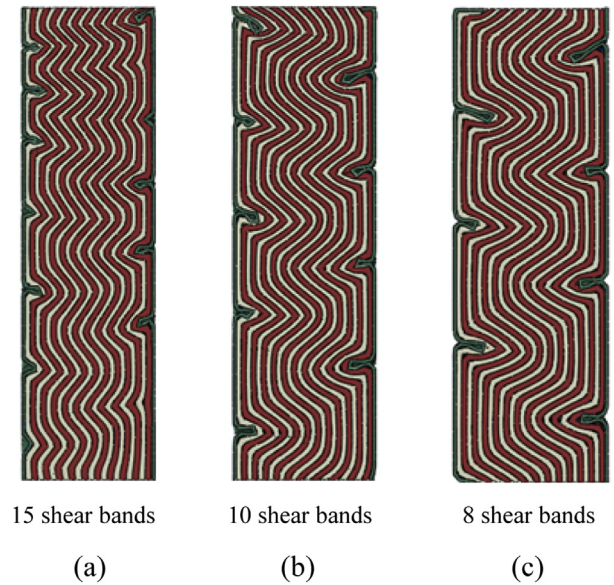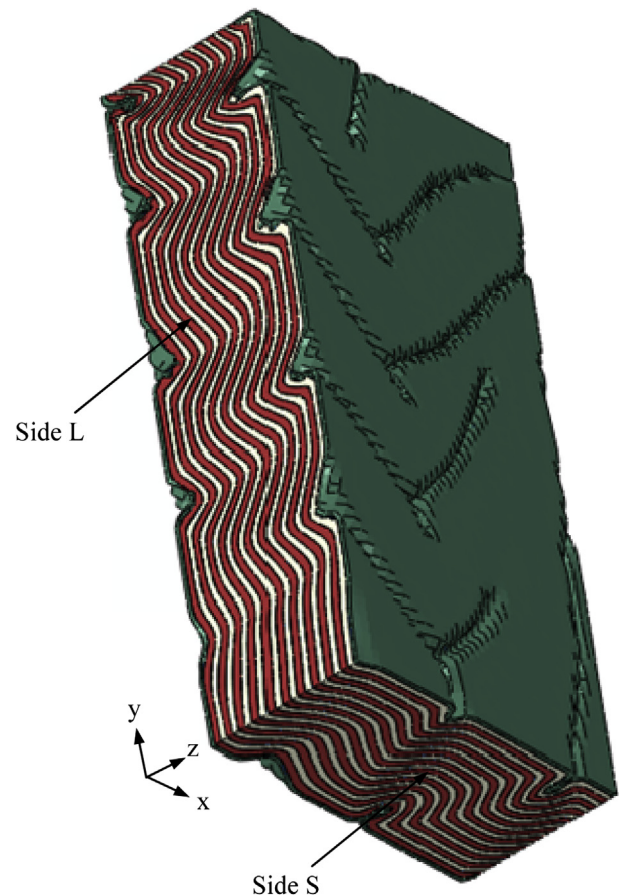

Fig. 16. The deformation pattern of the cell RVE specimen under equal biaxial constrained compression based on the model shown in Fig. 10(a) at the nominal strain of 22% in the x and y directions.

mechanism to accommodate the compression starts with the elastic buckling of the cell components. When a cell RVE specimen is under in-plane constrained compression, the component sheets buckle independently with the lateral constraints from the neighbor component sheets as indicated in Ref. [17]. Since the component sheets were only packed together, each component sheet can be treated as an individual sheet or thin plate under in-plane compression with the lateral constraints which can be treated as unattached elastic foundations.

For the anode, cathode and separator sheets in the middle portion of the cell RVE specimens, the buckling mode will be dominated by the constraints on both sides of the sheets. Lai et al. [17] presented the buckling load solutions for the cell RVE specimens by treating the cell component as a uniform straight beam supported by two equal unattached elastic foundations under end loads with both ends hinged based on the solution listed in Refs. [23,24]. The cover sheets have only one unattached elastic foundation and are free to buckle to the unconstrained side due to the small clearances in the die for the cell RVE specimen during the test. However, the small clearances will limit the cover sheets to fully develop a lower order buckling mode. For the neighbor anode, cathode and separator sheets near the cover sheets, they can start to buckle in a lower order mode with the cover sheets but will also be constrained by the rigid walls through the cover sheets. The detailed results of the finite element analyses indicate that the cover sheets and the neighbor anode, cathode and separator sheets are constrained by the rigid walls and buckle in a high order mode.

Therefore, treating the cover sheet as a beam with one unattached elastic foundation on one side and a small or zero clearance to a rigid wall on the other side appears to be a reasonable approach to gain insight on the buckling behavior and the number of the waves or half waves for the cell RVE specimens. The details of an elastic Rayleigh–Ritz buckling analysis are presented in Appendix A. The results of the elastic buckling analysis indicate that the number of waves, *n*, is proportional to the length *l* of the cell. In other words, the wavelength of the buckling is independent of the specimen length *l*. Since the cell RVE specimens buckle with multiple half waves, the selection of the length for the cell RVE specimens to represent lithium-ion battery cells with a full length under in-plane constrained compressive loading conditions in Lai et al. [17] appears to be reasonable.

8. Conclusions

In this paper, computational models are developed for simulations of representative volume element (RVE) specimens of lithium-ion battery cells under in-plane constrained compression tests. First, the load–displacement data and deformation patterns for cell RVE specimens under in-plane constrained compression tests are briefly reviewed. For the corresponding finite element analyses based on ABAQUS, the effective compressive moduli for cell components are obtained from in-plane constrained compressive tests, the Poisson's ratios for cell components are based on the rule of mixture, and the stress–plastic strain curves of the cell components are obtained from the tensile tests and the rule of mixture. The Gurson's material model is adopted to account for the effect of porosity in separators and in the active layers of anodes and cathodes. The computational results show that the computational models can be used to examine the micro buckling of the component sheets, the macro buckling of the cell RVE specimens, and the formation of the kinks and shear bands observed in experiments, and to simulate the load–displacement curves of the cell RVE specimens. The computational results also suggest the micro buckling of the component sheets controls the macro

buckling of the cell RVE specimens and then the formation of the kinks and shear bands. The initial micro buckling mode of the cover sheets in general agrees with that of the approximate elastic buckling solution of a beam with a rigid boundary on one side and an unattached elastic foundation on the other side. The elastic buckling solution indicates that the buckling wavelength is a function of the elastic bending rigidity and the out-of-plane elastic modulus of the cell RVE specimens. The results further suggest that the length of the cell RVE specimens is appropriately selected and the constrained compressive behavior of the cell RVE specimens can represent that of battery cells with a full length. Based on the computational models, the effects of the friction between the cell components and the constrained surfaces on the deformation pattern, plastic deformation, void compaction, and the load–displacement curve are identified. Finally, the usefulness of the computational model is demonstrated by further exploring the effects of the initial clearance and biaxial compression on the deformation patterns of cell RVE specimens.

Appendix A. Buckling of a beam on an elastic foundation and rigid boundary

Fig. A1 shows a uniform straight beam under end loads and with one unattached elastic foundation on one side and a rigid boundary on the other side. Both ends are hinged and the beam is supported by the elastic foundation through the lateral pressure proportional to the deflection in the *y* direction. Here, *k* represents the spring constant of the elastic foundation on one side of the beam and is defined as the lateral force per unit plate length per unit deflection of the neighbor components in the out-of-plane direction. The spring constant *k* can be expressed in terms of the out-of-plane elastic modulus *E* of the cell RVE specimens as

$$k = \frac{Eb}{h} \tag{A1}$$

where *b* represents the width of the specimen, and *h* represents the thickness of the neighbor components.

In calculating the critical value of the compressive force for a beam with an unattached elastic foundation on one side and a rigid boundary on the other side, the energy method can be used to develop an approximate solution [24]. The potential energy function for the beam can be expressed in terms of the strain energy of beam bending, the strain energy of the elastic foundation, and the work done by the compressive force as

$$\Pi = \frac{EI}{2} \int_0^l \left(\frac{\mathrm{d}^2 v}{\mathrm{d}x^2}\right)^2 \mathrm{d}x + \frac{k}{2} \int_0^l v^2 \mathrm{d}x - \frac{P}{2} \int_0^l \left(\frac{\mathrm{d}v}{\mathrm{d}x}\right)^2 \mathrm{d}x \tag{A2}$$

where Π is the potential energy of the system, *E* is the modulus of elasticity of the beam, *I* is the moment of inertia of the beam, *v* represents the deflection of the beam in the *y* direction, *l* is the length of the beam, *k* is the spring constant for the elastic unattached foundation, and *P* is the compressive force. Note that

the friction effects are not considered in this simple beam analysis.

According to the computational results for the cell RVE specimens with a small or zero tolerance in the die, the buckling mode appears to be periodic. The deflection v of the beam must be positive due to the rigid boundary on the left side as shown in Fig. A1. The deflection v is assumed in a form as

$$v = a_n \sin^2\left(\frac{n\pi x}{l}\right) \tag{A3}$$

where n is an integer and a_n is a coefficient. Substituting the deflection v in equation (A3) into equation (A2) and evaluating the integrals, the potential energy becomes

$$\Pi = a_n^2\left(EI\frac{n^4\pi^4}{l^3} + \frac{3}{16}kl - \frac{Pn^2\pi^2}{4l}\right) \tag{A4}$$

For the minimum potential energy, the critical buckling load is determined at $\partial\Pi/\partial a_n = 0$ as

$$P = \frac{4EI\pi^2}{l^2}\left(n^2 + \frac{3}{16}\frac{kl^4}{n^2\pi^4EI}\right) \tag{A5}$$

where the integer n represents the number of waves as indicated in equation (A3). It should be noted that in the buckling analysis in Lai et al. [17], the value of m corresponds the number of half waves for the buckling of the entire cell RVE specimens or the number of half waves of the anode, cathode and separator sheets in the middle portion of the cell RVE specimens.

Following the argument presented in Ref. [24] with consideration of n as an integer, the value of n at which the number of waves changes from n to $n+1$ giving the same value of P can be obtained from equation (A5) as

$$n^2(n+1)^2 = \frac{3}{16}\frac{kl^4}{\pi^4EI} \tag{A6}$$

The solution for equation (A6) is expressed as

$$n = \frac{1}{2}\left(\sqrt{1 + 4\frac{l^2}{\pi^2}\sqrt{\frac{3}{16}\frac{k}{EI}}} - 1\right) \tag{A7}$$

Equation (A7) is similar to the solution for the number of half waves for the buckling of a beam supported by an attached or unattached elastic foundation as listed in Timoshenko [24] and used in Lai et al. [17].

Equation (A5) is plotted in Fig. A2 to demonstrate the change of the compressive load P with n using the values of k, l, E and I that are listed in Table A1 based on the experimental results presented in Lai et al. [17]. Since n is an integer, equation (A5) is discrete in nature. Fig. A2 shows that the solution of n of 12 in equation (A7) corresponds to the minimum or critical buckling load for the beam. However, when n is treated as a real number, equation (A5) becomes differentiable and the value of n at which the minimum or critical compressive load P can be determined. Therefore, considering n as a real number, $\partial P/\partial n = 0$ gives

$$n = \left(\frac{3k}{16EI}\right)^{\frac{1}{4}}\frac{l}{\pi} \tag{A8}$$

It should be noted that when 1 is neglected on the left hand side of equation (A6) for large n's, equation (A6) becomes equation (A8). For the value of n in equation (A8), the minimum or critical buckling load P_c can be determined as

$$P_c = 2\sqrt{3}(kEI)^{\frac{1}{2}} \tag{A9}$$

Equations (A7) and (A8) give the values of n 11.62 and 12.11, respectively, based on the values of k, l, E and I that are listed in Table A1 and are obtained from the experimental results presented in Ref. [17]. Both equations give the same number of waves of 12 for the cover sheets for the minimum or critical buckling load. From the computational results for the cell specimen with the zero clearance, the number the waves for the initial buckling mode of the cover sheets is 8 which is comparable to the approximate solution obtained from the Rayleigh–Ritz method presented above. Equation (A8) appears to be a reasonable estimation for the current investigation and simple enough to show that the number of waves, n, is proportional to the length l of the cell.

Equation (A8) can be rewritten as

$$\frac{l}{n} = \left(\frac{16EI}{3k}\right)^{\frac{1}{4}}\pi \tag{A10}$$

As indicated in equation (A10), the wavelength, l/n, is independent of the specimen length. For the cell RVE specimens with the small clearance of 0.358 mm, the number of half waves for the buckling for the entire cell specimen is 7 and 10 from experimental and computational results, respectively. The computational results also show that as the clearance increases, the number of half waves decreases. Since the cell RVE specimens buckle with multiple half waves, the selection of the length for the cell RVE specimens in the experimental investigation of Lai et al. [17] appears to be reasonable based on equation (A10).
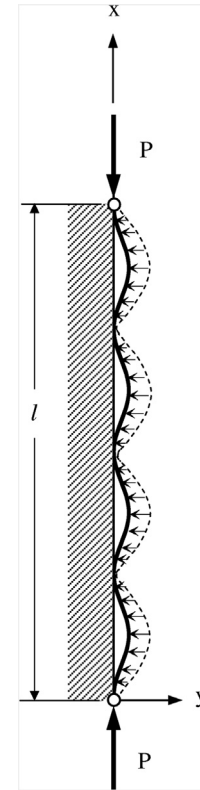

Fig. A1. A schematic of a uniform straight beam with a rigid boundary on one side and an unattached elastic foundation on the other side under end loads. Both ends are hinged and the beam is supported by the elastic foundation through the lateral pressure proportional to the deflection in the y direction.
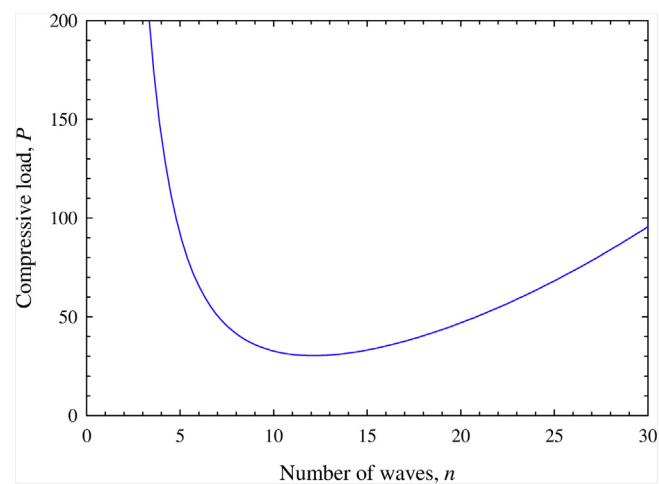
Fig. A2. The compressive load P as a function of the number of waves, n.

Table A1

The values of the parameters for the cell RVE specimens used in the elastic buckling solution for calculation of the critical buckling load and the number of waves.

Parameters	Value
$h_{\text{cover sheet}}$	0.111 mm
h_{anode}	0.200 mm
h_{cathode}	0.200 mm
$h_{\text{separator}}$	0.020 mm
$h_{\text{foundation}} = 10h_{\text{anode}} + 10h_{\text{cathode}} + 21h_{\text{separator}} + 1h_{\text{cover sheet}}$	4.531 mm
$E(=E_{\text{cover sheet}})$	575 MPa
$I\left(=I_{\text{cover sheet}}\right) = \dfrac{bh^3_{\text{cover sheet}}}{12}$	2.85E-03 mm^4
$b(=b_{\text{cell}})$	25 mm
$l(=l_{\text{cell}})$	25 mm
E_{cell} (from out-of-plane cell RVE compression tests)	8.5 MPa
Equation (A1): $k = \dfrac{E_{\text{cell}}b}{h_{\text{foundation}}}$	46.899 MPa

References

[1] J. Nguyen, C. Taylor, Safety performance for phosphate based large format lithium-ion battery, Telecommunications Energy Conference, INTELEC 2004. 26th Annual International (2004) 146–148.

[2] M. Otsuki, T. Ogino, K. Amine, ECS Transactions 1 (2006) 13–19.

[3] C. Ashtiani, Design and development for production of the think EV battery pack, Proceeding of the AABC-09 Conference (2009) CA, USA.

[4] J. Oh, Large lithium-ion battery for automotive applications, Proceeding of the AABC-09 Conference (2009) CA, USA.

[5] W. Cai, H. Wang, H. Maleki, J. Howard, E. Lara-Curzio, Journal of Power Sources 196 (2011) 7779–7783.

[6] X. Zhang, W. Shyy, A.M. Sastry, Journal of the Electrochemical Society 154 (10) (2007) A910–A916., http://dx.doi.org/10.1149/1.2759840.

[7] X. Zhang, A.M. Sastry, W. Shyy, Journal of the Electrochemical Society 155 (7) (2008) A542–A552., http://dx.doi.org/10.1149/1.2926617.

[8] R. Deshpande, Y.-T. Cheng, M.W. Verbrugge, Journal of Power Sources 195 (2010) 5081–5088., http://dx.doi.org/10.1016/j.jpowsour.2010.02.021.

[9] Y. Hu, X. Zhao, Z. Suo, Journal of Materials Research 25 (2010) 1007–1010.

[10] X. Xiao, W. Wu, X. Huang, Journal of Power Sources 195 (2010) 7649–7660.

[11] L.Q. Zhang, X. Liu, Y. Liu, S. Huang, T. Zhu, L. Gui, S. Mao, Z. Ye, C. Wang, J.P. Sullivan, J.Y. Huang, ACS Nano 5 (2011) 4800–4809.

[12] K. Zhao, W.L. Wang, J. Gregoire, M. Pharr, Z. Suo, J.J. Vlassak, E. Kaxiras, Nano Letters 11 (2011) 2962–2967., http://dx.doi.org/10.1021/nl201501s.

[13] K. Zhao, M. Pharr, L. Hartle, J.J. Vlassak, Z. Suo, Journal of Power Sources 218 (2012) 6–14., http://dx.doi.org/10.1016/j.jpowsour.2012.06.074.

[14] E. Sahraei, R. Hill, T. Wierzbicki, Journal of Power Sources 201 (2012) 307–321., http://dx.doi.org/10.1016/j.jpowsour.2011.10.094.

[15] R. Hill, Development for a Representative Volume Element of Lithium-Ion Batteries for Thermo-Mechanical Integrity, Department of Mechanical Engineering, Massachusetts Institute of Technology, 2011.

[16] E. Sahraei, T. Wierzbicki, R. Hill, M. Luo, Crash safety of lithium-ion batteries towards development of a computational model, SAE Technical Paper 2010-01-1078 (2010), http://dx.doi.org/10.4271/2010-01-1078.

[17] W. Lai, M.Y. Ali, J. Pan, Journal of Power Sources (2013) (submitted for publication).

[18] W. Lai, M.Y. Ali, J. Pan, Journal of Power Sources (2013) (submitted for publication).

[19] M.Y. Ali, W. Lai, J. Pan, Journal of Power Sources (2013) (submitted for publication).

[20] ABAQUS Version 6.11 User Manual, SIMULIA (2012). Providence, RI.

[21] A.L. Gurson, Journal of Engineering Materials and Technology 99 (1977) 2–15.

[22] V. Tvergaard, International Journal of Fracture Mechanics 17 (1981) 389–407.

[23] W.C. Young, R.G. Budaynas, Roark's Formulas for Stress and Strain, seventh ed., McGraw-Hill, 2001.

[24] S. Timoshenko, Theory of Elastic Stability, McGraw-Hill, 1936.